高等学校化学学报
CHEMICAL JOURNAL OF CHINESE UNIVERSITIES
研究论文

红光发射线粒体靶向铁掺杂碳点通过类过氧化物酶活性诱导铁死亡进行肿瘤治疗

薛小矿[1,2], 李　建[1,2], 梁焕仪[1,2], 王一颖[3], 葛介超[1,2]
(1. 中国科学院理化技术研究所, 北京 100190;
2. 中国科学院大学未来技术学院, 北京 100049; 3. 天津市人民医院感染管理处, 天津 300122)

摘要　合成了具有强类过氧化物酶活性的铁掺杂碳点(Fe-CDs), 将其用于肿瘤特异性治疗. Fe-CDs固有的红色荧光能够实现高对比度的细胞成像, 表明其聚集在线粒体. 在富含过氧化氢(H_2O_2)的酸性肿瘤微环境中, Fe-CDs能催化羟基自由基(•OH)生成, 诱导脂质过氧化, 最终触发铁死亡. 体内外实验均表明, Fe-CDs对肿瘤生长具有显著的抑制作用. 此外, Fe-CDs表现出优异的生物相容性, 未见明显的全身毒性. 通过结合荧光成像与催化治疗, 本研究为肿瘤治疗和铁死亡研究提供了一个有前景的新策略.

关键词　碳点; 纳米酶; 线粒体靶向; 铁死亡; 肿瘤治疗
中图分类号　O636　　**文献标志码**　A　　doi: 10.7503/cjcu20250094

Red-emissive Mitochondria-targeting Iron-doped Carbon Dots for Tumor Therapy *via* Peroxidase-mimicking Activity-induced Ferroptosis

XUE Xiaokuang[1,2], LI Jian[1,2], LIANG Huanyi[1,2], WANG Yiying[3*], GE Jiechao[1,2*]
(*1. Technical Institute of Physics and Chemistry, Chinese Academy of Sciences, Beijing* 100190, *China*;
2. School of Future Technology, University of Chinese Academy of Sciences, Beijing 100049, *China*;
3. Infection Prevention and Control Department of Tianjin People's Hospital, Tianjin 300122, *China*)

Abstract　In this work, iron-doped carbon dots(Fe-CDs) with strong peroxidase-mimicking activity were synthesized for tumor-specific therapy. Their intrinsic red fluorescence enabled high-contrast cellular imaging, revealing preferential mitochondrial accumulation. In the acidic and hydrogen peroxide(H_2O_2)-rich tumor microenvironment, Fe-CDs catalyzed hydroxyl radical(•OH) generation, inducing oxidative stress and lipid peroxidation, ultimately triggering ferroptosis. *In vitro* and *in vivo* studies demonstrated potent tumor inhibition. Furthermore, Fe-CDs exhibited excellent biocompatibility with no significant systemic toxicity. By integrating fluorescence imaging and catalytic therapy, this study presents a promising nanoplatform for tumor treatment and ferroptosis research.

Keywords　Carbon dots; Nanozyme; Mitochondria-targeting; Ferroptosis; Tumor therapy

收稿日期: 2025-03-31. 网络首发日期: 2025-04-28.
联系人简介: 王一颖, 男, 硕士, 副主任医师, 主要从事新型消毒材料研发方面的研究. E-mail: therediceberg@163.com
葛介超, 男, 博士, 研究员, 主要从事功能纳米材料在生物医学、能源环境方面的应用研究. E-mail: jchge2010@mail.ipc.ac.cn
基金项目: 国家重点研发计划项目(批准号: 2022YFA1207600)和国家自然科学基金(批准号: 52272052)资助.
Supported by the National Key Research and Development Program of China(No. 2022YFA1207600) and the National Natural Science Foundation of China(No. 52272052).

1 Introduction

Nanozymes, a class of nanomaterials with enzyme-mimetic catalytic activity, have attracted considerable attention in tumor therapy due to their high stability, tunable catalytic properties, and tumor microenvironment responsiveness[1,2]. Among them, peroxidase (POD)-like nanozymes have shown great potential by catalyzing the decomposition of hydrogen peroxide (H_2O_2) into highly toxic hydroxyl radicals (•OH), triggering oxidative stress and inducing tumor cell death[3~5]. Compared to natural enzymes, nanozymes offer improved stability, cost-effectiveness, and controllability[6~9]. Huo *et al.*[10] reported a tumor microenvironment-responsive nanozyme that selectively generates •OH in acidic conditions, leading to remarkable tumor therapeutic efficacy. Fan *et al.*[11] reported an N-doped carbon-based nanozyme with multiple enzyme-mimicking activities, including POD-mimic activity. By incorporating ferritin, the nitrogen-doped porous carbon nanospheres were directed to lysosomes, where they promoted tumor-specific reactive oxygen species (ROS) generation, leading to significant tumor regression in a human tumor xenograft mouse model. However, many existing nanozymes' therapeutic mechanisms, particularly in regulating specific cell death pathways, remain insufficiently explored.

Mitochondria play a crucial role in cellular metabolism, oxidative stress regulation, and programmed cell death[12]. Ferroptosis, an iron-dependent form of cell death characterized by ROS accumulation and lipid peroxidation, has gained increasing attention as a promising anti-cancer strategy[13~15]. Since mitochondria are key regulators of oxidative stress, targeting them with catalytic nanozymes could enhance therapeutic efficacy by amplifying ROS production and lipid peroxidation[16]. Wu *et al.*[17] reported a Fe_3S_4 nanozyme that effectively inhibited tumor growth by inducing ferroptosis and apoptosis in tumor cells through POD-mimicking activity-mediated ROS generation. However, the intrinsic lack of fluorescence in these nanozymes poses challenges for subcellular imaging and the study of cell death mechanisms. Engineering nanozymes with strong catalytic activity and organelle-specific localization are therefore critical for improving therapeutic precision and unraveling ferroptosis mechanisms.

Carbon dots (CDs), a class of zero-dimensional carbon-based nanomaterials, have attracted significant attention due to their unique optical properties, biocompatibility, and tunable surface chemistry[18~20]. CDs typically exhibit strong fluorescence, excellent photostability, and low cytotoxicity, making them promising candidates for bioimaging, biosensing, and drug delivery applications[21~23]. Moreover, by incorporating heteroatoms such as nitrogen or sulfur, CDs can be engineered to possess enzyme-mimicking catalytic activities, expanding their potential in therapeutic applications. In particular, some CDs have demonstrated peroxidase-like activity, enabling the catalytic decomposition of hydrogen peroxide into highly reactive •OH[24~26]. This feature, combined with their ability to accumulate in specific subcellular organelles, positions CDs as promising agents for tumor microenvironment-responsive catalytic therapy and oxidative stress-mediated cancer treatment.

In this work, we synthesized iron-doped carbon dots (Fe-CDs) with intrinsic red fluorescence and POD-mimicking activity for tumor therapy (Scheme 1). Their red fluorescence enabled high-contrast cellular imaging, while their selective mitochondrial accumulation facilitated localized •OH generation in the acidic, H_2O_2-rich tumor microenvironment[27]. This oxidative stress induced lipid peroxidation disrupted mitochondrial function, and triggered ferroptosis. *In vitro* and *in vivo* studies demonstrated significant tumor suppression, while biocompatibility assessments confirmed minimal systemic toxicity. By integrating fluorescence imaging and catalytic therapy into a single nanoplatform, this study provides a promising strategy for precision tumor treatment and ferroptosis research.

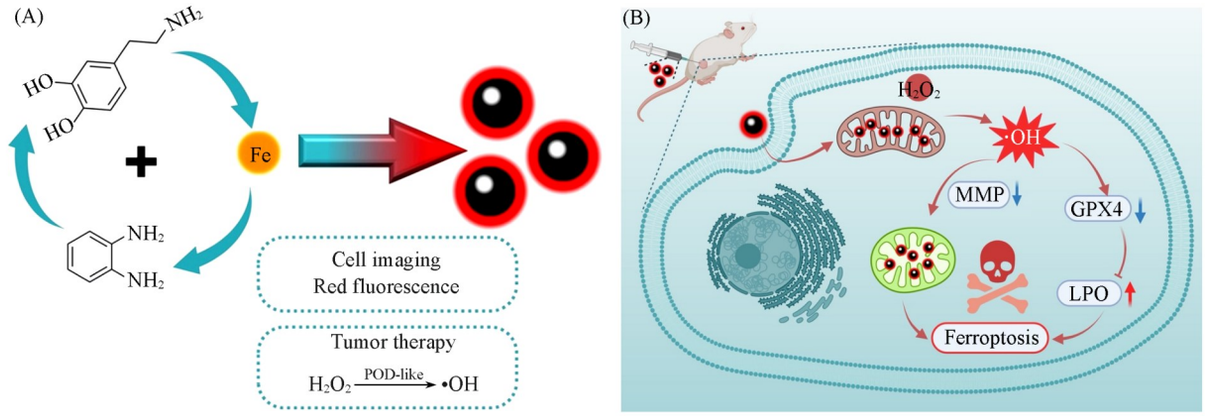

Scheme 1 Schematic of the synthesis process of Fe-CDs(A) and the illustration of Fe-CDs for cell imaging and tumor therapy(B)

2 Experimental

2.1 Materials and Measurements

All chemical reagents were used as received without further purification unless otherwise stated. *O*-phenylenediamine (OPD), ferric chloride hexahydrate, 2,2′-Azino-bis(3-ethylbenzothiazoline-6-sulfonic acid) (ABTS), 3,3′,5,5′-Tetramethylbenzidine(TMB), and disodium terephthalate(NaTA) were purchased from Innochem(Beijing, China). MTT assay kits, Calcein-AM/PI kits, dihydroethidium(DHE), 2′,7′-dichlorodihydrofluorescein diacetate(DCFH-DA), 3′-*p*-(hydroxyphenyl) fluorescein(HPF), lysosomal fluorescence probes, mitochondrial fluorescence probes, and JC-1 probes were obtained from Beyotime Biotechnology (Shanghai, China). The lipid peroxidation probe(LPO) was purchased from Dojindo(Japan).

2.2 Synthesis of Fe-CDs

Fe-CDs were synthesized *via* a solvothermal method. Specifically, 0.1 g of o-phenylenediamine and 0.1 g of dopamine hydrochloride were completely dissolved in 10 mL of anhydrous ethanol, while 0.05 g of ferric chloride hexahydrate was dissolved in 5 mL of anhydrous ethanol. The two solutions were then mixed thoroughly and transferred into a Teflon-lined autoclave, followed by heating at 180 ℃ for 12 h. After naturally cooling to room temperature, the reaction mixture was centrifuged at 14000 r/min to remove the supernatant. The precipitate was washed three times with anhydrous ethanol. The obtained precipitate was redispersed in water and dialyzed using a 3500 Da dialysis membrane for 24 h. The resulting solution was then lyophilized for further characterization.

2.3 Characterization of Fe-CDs

The transmission electron microscopy(TEM) and high-resolution TEM(HRTEM) images were performed on HT7700 and a JEM-2100 field-emission electron microscope(Hitachi, Japan). Fourier transform infrared spectra(FTIR) were recorded on an Excalibur 3100 spectrophotometer(Varian, USA). X-ray photoelectron spectroscopy(XPS) analyses(Thermal Instruments Inc., USA). UV-Vis absorption spectra were acquired on a U-3900 UV-Vis spectrophotometer(Hitachi, Japan). Fluorescence spectra were obtained from F-4800 fluorescence spectrophotometer(Hitachi, Japan). Cell imaging was performed using a Nikon A1 confocal laser scanning microscope(CLSM, Nikon, Japan).

2.4 Measurement of •OH by POD-mimicking Activity

The NaTA photoluminescence assay was employed to detect the generation of •OH. A reaction mixture containing 5 mmol/L H_2O_2, 1 mmol/L NaTA, and Fe-CDs were prepared in 0.1 mol/L HAc-NaAc buffer(pH=4.5). The fluorescence intensity of the mixture was monitored using a fluorescence spectrophotometer for

5 min.

The POD-mimicking activity was also evaluated using OPD, ABTS, and TMB. A reaction mixture containing 5 mmol/L H_2O_2, 1 mmol/L indicator(OPD, ABTS, or TMB), and Fe-CDs were prepared in 0.1 mol/L HAc-NaAc buffer(pH=4.5). The absorbance of the mixture was monitored for 5 min.

The steady-state kinetic assay of Fe-CDs using H_2O_2 as the substrate was conducted in the presence of 1.0 mmol/L TMB and varying concentrations of H_2O_2(1, 2, 3, and 4 mmol/L). Similarly, the steady-state kinetic assay using TMB as the substrate was performed in the presence of 1.0 mmol/L H_2O_2 and different concentrations of TMB(0.2, 0.4, 0.6, 0.8, and 1.0 mmol/L). The absorbance of ox-TMB at 655 nm was measured using a UV-Vis spectrophotometer at different time points. Catalytic parameters were determined based on the Michaelis-Menten equation[Eq.(1) and Eq.(2)][28].

$$v = \frac{v_{max}[s]}{K_M + [s]} \tag{1}$$

$$\frac{1}{v} = \frac{K_M}{v_{max}[s]} + \frac{1}{v_{max}} \tag{2}$$

In the equation, v is the rate of conversion, v_{max} is the maximum rate of conversion, [s] is the concentration of substrate and K_M is the Michaelis constant.

For the electron paramagnetic resonance (ESR) assay, BMPO was used as the ROS trapping agent. Fe-CDs and 1.0 mmol/L H_2O_2 were added into the HAc-NaAc buffer(0.1 mol/L, pH=4.5) to detect the generation of •OH.

2.5 Cell Culture

Three kinds of cell lines were involved in this study. HUVEC and HeLa cells were cultured in DMEM containing 10% FBS and 1% penicillin. 4T1 was cultured in RPMI-1640 medium with 10% FBS and 1% penicillin. All cells were incubated in an incubator at 37 ℃ with 5% CO_2.

2.6 Cell Imaging

HeLa cells seeded in 35 mm cell culture dishes were incubated with Fe-CDs for different durations. After incubation, the cells were carefully washed with PBS to remove excess Fe-CDs and subsequently imaged using a Nikon A1 CLSM.

2.7 Intracellular ROS Detection

HeLa cells seeded in 35 mm cell culture dishes were incubated with Fe-CDs under different conditions. After 12 h of incubation, the culture medium was replaced with DMEM, and adjusted to pH=6.5 using PIPES. HPF(10 μL, 1 mmol/L) or DCFH-DA(10 μL, 1 mmol/L) was then added for staining, followed by a 30 min incubation. Fluorescence images of HeLa cells were subsequently acquired using Nikon A1 CLSM.

2.8 Cytotoxicity *In Vitro*

Different cells were seeded into a 96-well plate and incubated for 24 h. Following different treatments, the culture medium was removed, and a 10% MTT solution(prepared in medium) was added, followed by incubation for 2—4 h. Subsequently, DMSO was added to dissolve the formed formazan crystals. The absorbance was then measured at 570 nm using a microplate reader.

2.9 Calcein AM/PI Assays

Approximately 10^5 4T1 cells were seeded into glass-bottom culture dishes and incubated for 24 h. The cells were then divided into different treatment groups: no treatment, H_2O_2(100 μmol/L), co-incubation with Fe-CDs, and co-incubation with Fe-CDs and H_2O_2(100 μmol/L). After replacing the medium with a fresh culture medium, the cells were incubated overnight. Following medium removal, the cells were co-stained with Calcein AM and PI for 30 min. After three washes with PBS, fluorescence images were acquired using Nikon A1 CLSM.

2.10 Subcellular Colocalization Analysis

4T1 cells were seeded in 35 mm confocal culture dishes and incubated for 12 h. After washing twice with PBS, the cells were subjected to different treatments. Following incubation, the cells were washed again with PBS and then stained with Mito-Tracker™ Green FM(100 nmol/L) for mitochondrial labeling or Lyso-Tracker™ Green DND-26(100 nmol/L) for lysosomal labeling. The staining process was carried out at 37 ℃ for 30 min in the dark, fluorescence images were captured using a Nikon A1 CLSM. Pearson's correlation coefficients for colocalization analysis were obtained using Nikon A1 confocal microscope software.

2.11 JC-1 Assay

4T1 cells were seeded in a 6-well plate and incubated for 12 h. After washing with PBS, the cells were subjected to different treatment conditions. They were then incubated with JC-1 dye(5 μg/mL) for 30 min in the dark. Following another PBS wash, fluorescence images were acquired using a Nikon A1 CLSM, with excitation at 488 nm for the green channel and 543 nm for the red channel.

2.12 Lipid Peroxidation(LPO) Assay

To evaluate lipid peroxidation levels, 4T1 cells were seeded in confocal culture dishes and incubated for 12 h. After different treatments, the cells were washed with PBS and then incubated with a lipid peroxidation probe(LPO, 5 μmol/L) at 37 ℃ for 30 min in the dark. Subsequently, the cells were carefully washed three times with PBS to remove the excess probe. Fluorescence images were acquired using a Nikon A1 CLSM.

2.13 Western Blot Analysis

4T1 cells were seeded on 6 well plates and incubated for 12 h. After washing with PBS, the cells were subjected to different treatments and further incubated overnight. The cells were then collected, lysed in a loading buffer, and heated at 99 ℃ for 5 min. The lysates were centrifuged at 12000 r/min for 10 min, and the supernatants were collected for protein analysis. Equal amounts of protein samples were separated on a 12% SDS-PAGE gel and transferred onto PVDF membranes at 200 mA for 40 min. The membranes were washed three times with TBST and blocked with either bovine serum albumin(BSA) or skim milk for 2 h at room temperature. After blocking, the membranes were incubated overnight at 4 ℃ with primary antibodies(1∶500 dilution) in a blocking solution. Following three 5-minute washes with TBST, the membranes were incubated with secondary antibodies(1∶3000 dilution) at room temperature for 1 h, followed by three additional TBST washes. Protein expression was detected using a chemiluminescent HRP substrate.

2.14 *In Vivo* Antitumor Efficacy

A tumor-bearing mouse model was established by subcutaneously injecting 5×10^5 4T1 cells into the upper dorsal region of female BALB/c mice. Once the tumors reached approximately 50 mm^3 in volume, the mice were randomly divided into two groups and received intratumoral injections of 100 μL PBS or Fe-CDs(n=5 per group). Tumor volumes were measured every two days and calculated using Eq.(3).

$$V_{\text{Tumor}} = \frac{(\text{Tumor length})(\text{Tumor width})^2}{2} \tag{3}$$

All mice were euthanized on the day 20 after the initial treatment.

2.15 *In Vivo* Biocompatibility Analysis

For histological evaluation, major organs(heart, liver, spleen, lungs, and kidneys) were harvested, fixed in tissue fixative, and embedded in paraffin. The organ sections were stained with hematoxylin and eosin (H&E) and subjected to immunohistochemical staining. Histological analysis was performed using an optical microscope. For blood analysis, serum and plasma were collected at the end of the *in vivo* experiments and assessed for complete blood count as well as liver and kidney function.

2.16 Statistical Analyses

The data presented are representative of at least three independent experiments. Statistical analyses were conducted using GraphPad Prism software. Comparisons between two groups were performed using Student's *t*-test, while comparisons among multiple groups were analyzed using one-way ANOVA, followed by the LSD-*t* test for further pairwise comparisons. (ns: not significant, * $P<0.05$, ** $P<0.01$, *** $P<0.001$, **** $P<0.0001$).

3 Results and Discussion

3.1 Synthesis and Characteristics of Fe-CDs

Fe-CDs were synthesized using a solvothermal method, transmission electron microscopy (TEM) images showed that Fe-CDs had an average diameter of approximately 10 nm. High-resolution TEM (HR-TEM) revealed their amorphous carbon structure, indicating partial graphitization [Fig. 1 (A)]. The UV-Vis absorption spectrum displayed broad absorption in the visible range [Fig. 1 (B)]. Photoluminescence spectra exhibited red fluorescence under various excitation wavelengths, highlighting their potential for subcellular imaging [Fig. 1 (C)].

The structural composition of Fe-CDs was further analyzed using Fourier transform infrared (FTIR) and

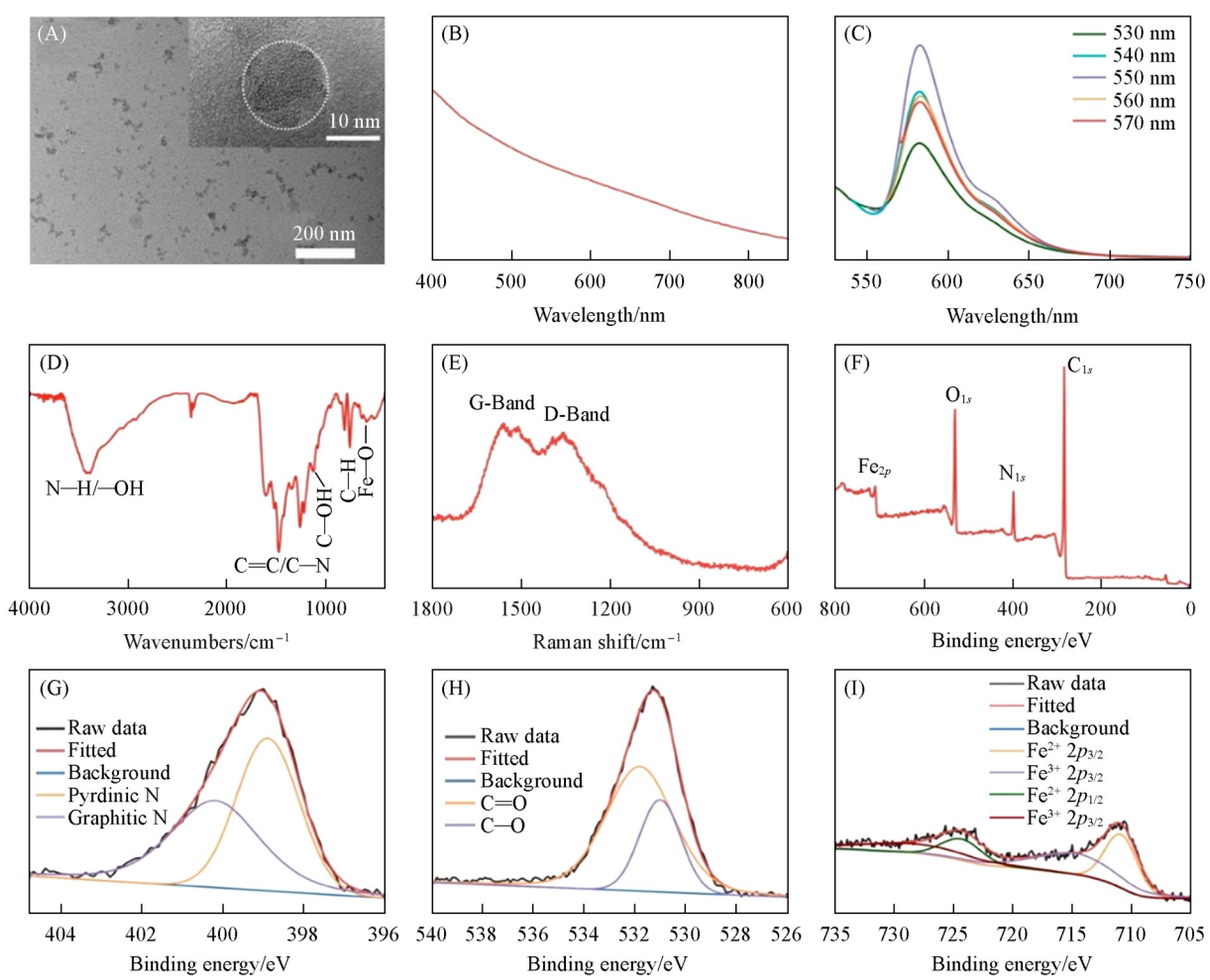

Fig. 1 Characterization of Fe-CDs

(A) TEM and HR-TEM images of Fe-CDs; (B) UV-Vis absorbance spectrum; (C) fluorescence emission spectra of Fe-CDs under excitation at different wavelengths; (D) FTIR spectrum; (E) raman spectrum; (F) XPS survey spectrum of Fe-CDs; high-resolution XPS spectra of N_{1s} (G), O_{1s} (H), and Fe_{2p} (I).

Raman spectroscopy. FTIR spectra[Fig.1(D)] revealed characteristic functional groups, with peaks at 3400 corresponding to N—H and O—H stretching vibrations, respectively. Peaks at 1050 and 800 cm^{-1} were assigned to C—OH and C—H, indicating the presence of oxygen- and nitrogen-containing groups in a conjugated aromatic framework[29]. Additionally, a peak at 570 cm^{-1} suggested catechol-Fe^{3+} coordination. Raman spectra confirmed the carbonaceous nature of Fe-CDs, displaying prominent D and G bands associated with sp^3 and sp^2 hybridized carbon, respectively[Fig.1(E)][30].

X-Ray photoelectron spectroscopy (XPS) provided further insights into the elemental composition and oxidation states of Fe-CDs [Fig. 1 (F)]. The primary constituents included C (68.28%, atomic ratio), O(16.75%), N(10.18%), and Fe(2.22%)[Table S1, in the Electronic Supplementary Information(ESI)]. The C_{1s} spectrum displayed peaks at 284.6, 286.0, and 288.4 eV, corresponding to C—C/C=C, C—N, and C=O/C=N bonds, confirming heteroatom doping (Fig. S1 in the ESI). Deconvolution of the N_{1s} spectrum revealed two peaks at 398.9 and 400.2 eV, attributed to pyrrolic N and graphitic N, respectively [Fig.1(G)]. The O_{1s} spectrum exhibited peaks at 531.0 and 531.9 eV, associated with C=O and C—OH/C—O—C groups, consistent with the C_{1s} analysis[Fig.1(H)]. The Fe_{2p} spectrum showed multiple peaks corresponding to Fe^{2+} and Fe^{3+}, indicating the coexistence of different oxidation states[Fig.1(I)][31,32].

3.2 POD-mimic Activities

Fe-doped nanomaterials have been reported to exhibit POD-mimicking activity *via* the heterogeneous Fenton reaction, wherein highly cytotoxic •OH was generated during the catalytic decomposition of H_2O_2[24,33]. To confirm the POD-mimicking activity of Fe-CDs, we first employed NaTA, a specific probe for •OH, to detect the characteristic product of POD-mimic activity[Fig.2(A)]. Under acidic conditions, NaTA was oxidized to 2-OH-TA by •OH, which exhibited a significant fluorescence increase at 450 nm over time[Fig.2(B)], indicating the POD-mimicking activity of Fe-CDs. Additionally, we utilized OPD [Fig.2(C)] and ABTS [Fig.2(E)], both of which undergo oxidation by •OH, resulting in absorbance changes. The results showed that OPD was oxidized to DAPN[Fig.2(D)], and ABTS was converted to $ABTS^{\cdot+}$[Fig.2(F) and Table S2 in the ESI] under acidic conditions, further confirming the POD-mimicking activity of Fe-CDs.

To strengthen this finding, we conducted a TMB oxidation assay [Fig.2(G)]. Upon co-incubation of Fe-CDs, H_2O_2, and TMB under acidic conditions, the colorless TMB was oxidized to a blue product, as evidenced by a prominent absorption peak at 652 nm[Fig.2(H)], confirming the formation of ox-TMB and further supporting the POD-mimicking activity of Fe-CDs. This result was also corroborated by ESR spectroscopy (Fig.S3 in the ESI), where a distinct 1∶2∶2∶1 peak of BMPO/OH was observed, providing the direct evidence for •OH generation.

To further investigate the POD-mimicking activity of Fe-CDs, we analyzed their Michaelis-Menten steady-state kinetics at varying H_2O_2 concentrations(1, 2, 3, and 4 mmol/L)[Fig.2(I)]. The corresponding Michaelis-Menten plot[Fig.2(J)] yielded a Michaelis constant(K_M) of 1.09 mmol/L and a maximum velocity (V_{max}) of 5.58×10^{-8} mol/(L·s). Similarly, steady-state kinetics were assessed at different TMB concentrations (0.2, 0.4, 0.6, 0.8, and 1 mmol/L)[Fig.2(K)], with the corresponding kinetic plot shown in Fig.2(L). The calculated K_M and V_{max} values were 0.44 mmol/L and 1.11×10^{-7} mol/(L·s), respectively, indicating that Fe-CDs exhibit superior POD-mimicking activity compared to Fe_3O_4[34].

We then investigated the effect of pH on the POD-mimicking activity of Fe-CDs by conducting TMB oxidation assays under different pH conditions(Fig.S4 in the ESI). As the pH decreased from 7.4 to 4.5, a more pronounced color change and a higher absorbance of ox-TMB were observed, indicating enhanced POD-mimicking activity in an acidic environment. This aligned well with the acidic and H_2O_2-rich characteristics of the tumor microenvironment, highlighting the great potential of Fe-CDs as a tumor microenvironment-responsive

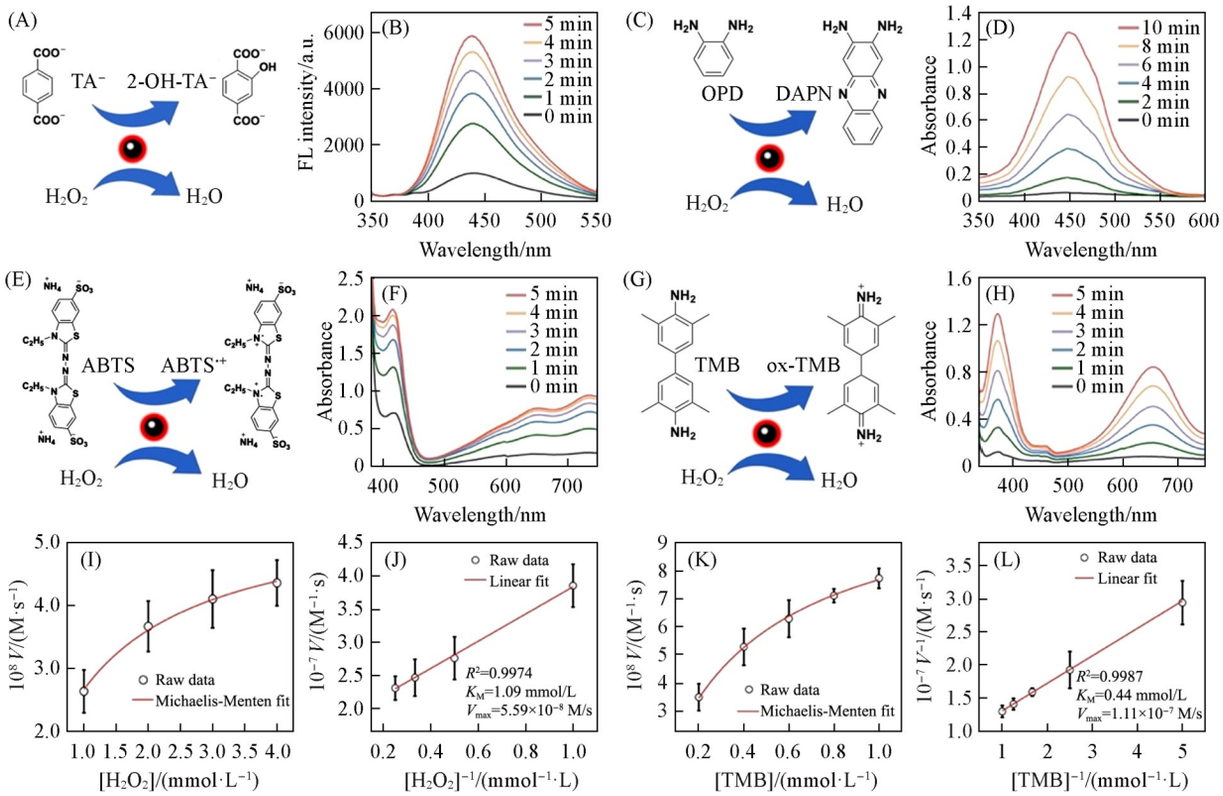

Fig. 2 POD-mimicking activity of Fe-CDs

Reaction equation(A) and Fluorescence spectra(B) of NaTA oxidized by •OH generated through the POD-mimicking activity of Fe-CDs in an acidic environment(pH=4.5); reaction equation(C) and absorbance spectra(D) of OPD oxidized by •OH generated through the POD-mimicking activity of Fe-CDs in an acidic environment(pH=4.5); reaction equation(E) and absorbance spectra(F) of ABTS oxidized by •OH generated through the POD-mimicking activity of Fe-CDs in an acidic environment(pH=4.5); reaction equation(G) and absorbance spectra(H) of TMB oxidized by •OH generated through the POD-mimicking activity of Fe-CDs in an acidic environment(pH=4.5); michaelis-Menten kinetic analysis(I) and Lineweaver-Burk plot(J) for Fe-CDs using H_2O_2 as the substrate; michaelis-Menten kinetic analysis(K) and Lineweaver-Burk plot(L) for Fe-CDs using TMB as the substrate.

therapeutic agent.

3.3 Intracellular ROS Detection and *In Vitro* Therapy

CLSM was used to investigate the uptake of Fe-CDs by HeLa cells. As shown in Fig.3(A), the red fluorescence within the cells gradually increased over time, indicating the internalization of Fe-CDs, reaching a peak at 6 h without significant attenuation at 12 h.

Furthermore, HPF was used to detect •OH generated by the POD-mimicking activity of Fe-CDs. As shown in Fig.3(B), under mildly acidic conditions simulating the tumor microenvironment, the Control and H_2O_2-only groups exhibited negligible green fluorescence in 4T1 cells, whereas the Fe-CDs-treated group showed a noticeable fluorescence increase. The highest fluorescence intensity was observed in the Fe-CDs and H_2O_2 co-incubation group, confirming that Fe-CDs can exploit tumor microenvironment-specific conditions to generate •OH within tumor cells. Similarly, DCFH fluorescence staining further verified the accumulation of Fe-CDs-induced ROS in tumor cells, providing a solid foundation for their potential application in tumor cell eradication.

Encouraged by the ROS generation capability of Fe-CDs *in vitro*, we evaluated their therapeutic efficiency using MTT assays. First, cytotoxicity tests on normal cells(HUVEC) showed no significant viability reduction even at 100 μg/mL, demonstrating good biocompatibility[Fig.3(C)]. In contrast, under weak acidic conditions mimicking the tumor microenvironment, 4T1 cell viability decreased sharply with increasing Fe-CDs

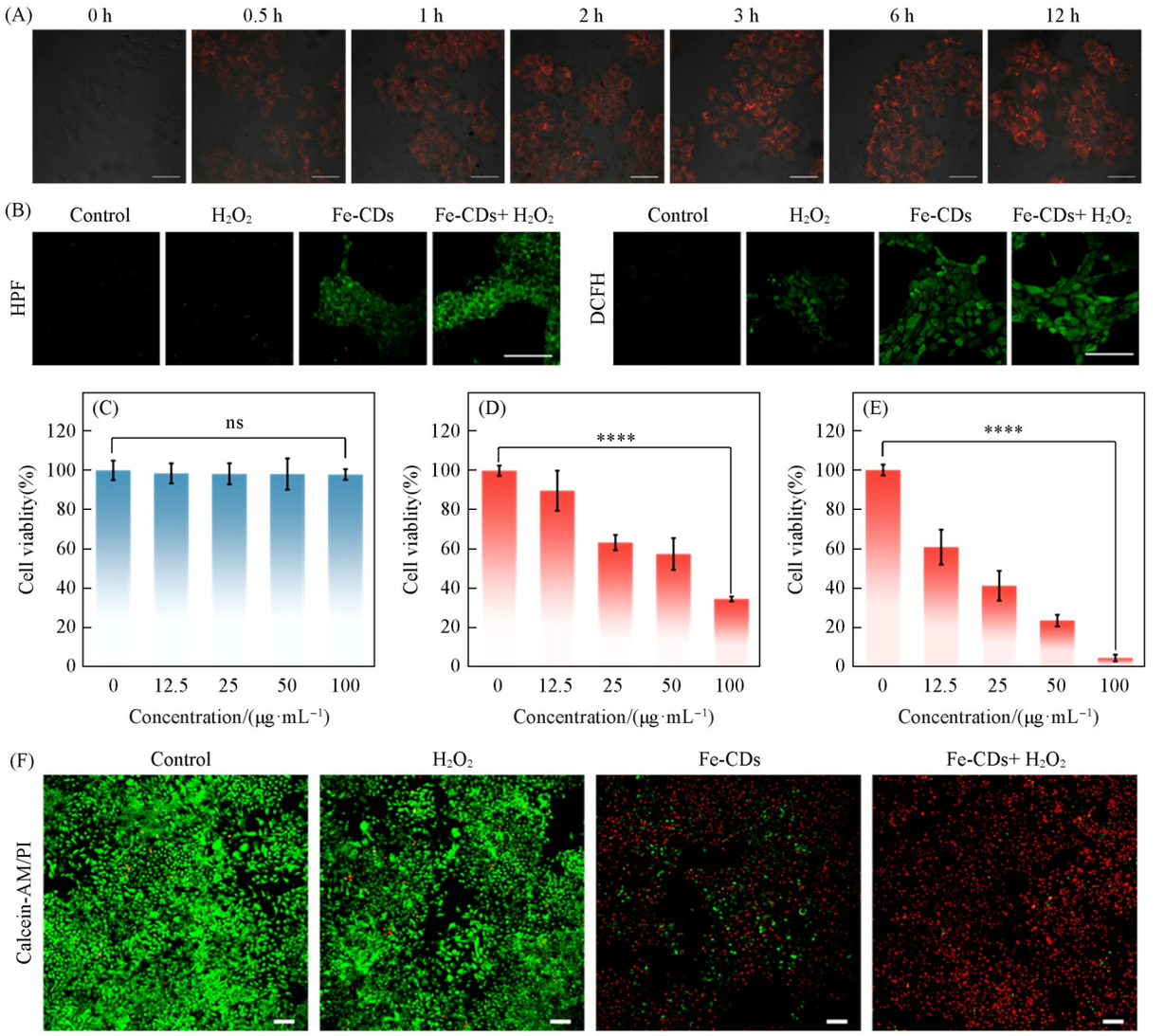

Fig. 3 Cellular imaging and *in vitro* cytotoxicity

(A) CLSM images of cells incubated with Fe-CDs for different durations (scale bar: 100 μm); (B) CLSM images of intracellular ROS generation under different treatments using HPF and DCFH as probes for •OH and total ROS, respectively (scale bar: 100 μm); (C) cell viability of HUVECs after 24 h incubation with Fe-CDs at different concentrations; (D) cell viability of 4T1 cells after 24 h incubation with Fe-CDs (culture medium adjusted to pH=6.5 using PIPES); (E) cell viability of 4T1 cells after 24 h incubation with Fe-CDs in a PIPES-buffered medium (pH=6.5) with 100 μmol/L H_2O_2; (F) CLSM images of live and dead 4T1 cells after different treatments (scale bar: 200 μm).

concentration, reaching 45% at 100 μg/mL [Fig.3(D)]. Remarkably, cell viability further dropped to 2.5% after adding trace H_2O_2 (100 μmol/L), attributable to the potent POD-mimic enzyme activity of Fe-CDs [Fig.3(E)]. Therapeutic efficacy was further verified through dual staining with Calcein-AM (live cells) and PI (dead cells) [Fig.3(F)]. The control and H_2O_2 groups exhibited strong green fluorescence without red signals, indicating minimal cell death. The Fe-CDs group showed both red and green fluorescence, suggesting partial cancer cell death. Strikingly, intense homogeneous red fluorescence revealed complete cancer cell eradication in the Fe-CDs and H_2O_2 co-incubation group. These results aligned well with MTT assay data, confirming Fe-CDs′ significant potential for catalytic cancer therapy.

3.4 Mechanism of mitochondrion-induced cell ferroptosis

Cellular uptake experiments demonstrated that Fe-CDs predominantly localized in the cytoplasm, with

no detectable accumulation in the nucleus[Fig.3(A)]. To further investigate their subcellular localization, colocalization assays were performed using commercially available fluorescent dyes, Lyso-Tracker Green and Mito-Tracker Green, as lysosomal and mitochondrial markers, respectively. As shown in the CLSM images [Fig.4(A) and(B)], Fe-CDs exhibited preferential accumulation in mitochondria(Rp=86%) following 6 h of incubation with 4T1 cells, whereas their presence in lysosomes was comparatively lower(Rp=51%). These results suggested that Fe-CDs possessed a notable affinity for mitochondria.

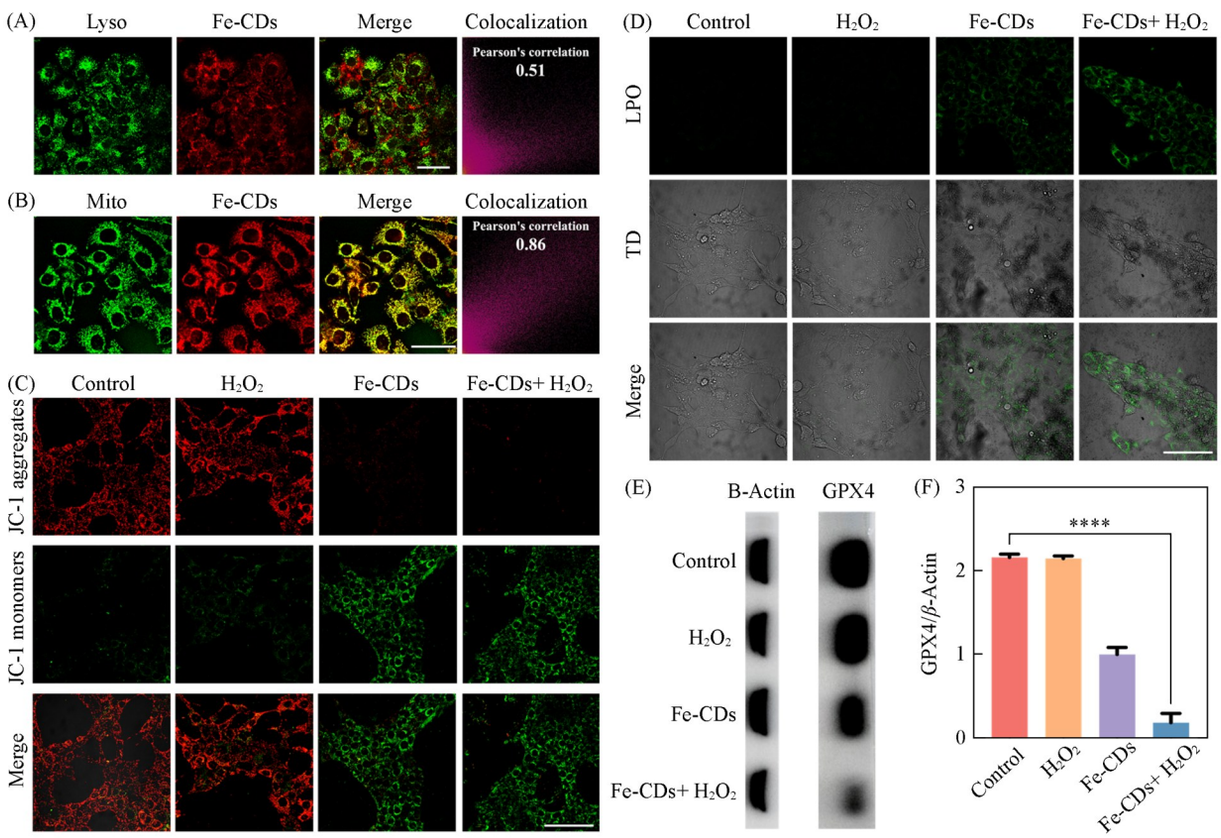

Fig. 4 Mechanism of mitochondrial dysfunction-induced tumor cell ferroptosis

CLSM images of Fe-CDs incubated with HeLa cells co-stained with Lyso-Tracker Green(A) and Mito-Tracker Green(B)(Scale bars: 25 μm); CLSM images of JC-1(C) and LPO stained 4T1 cells(D) after different treatments(Scale bars: 100 μm); Western blot(E) and quantitative analysis of protein expression(F) related to the mitochondrion-mediated ferroptosis pathway in 4T1 cells.

Mitochondrial membrane potential(MMP) is crucial for maintaining mitochondrial function, and its dissipation can lead to increased membrane permeability and mitochondrial dysfunction. Thus, JC-1 staining was employed to assess the effect of Fe-CDs on MMP in 4T1 cells. As depicted in Fig.4(C), untreated 4T1 cells exhibited intense red fluorescence, indicating intact mitochondrial membrane potential. In contrast, Fe-CD-treated cells showed partial green fluorescence, suggesting moderate mitochondrial depolarization. Notably, in the Fe-CDs and H_2O_2 co-incubation group, nearly all cells displayed green fluorescence, indicating a pronounced loss of MMP and severe mitochondrial dysfunction. Mitochondrial membrane damage is a key feature of ferroptosis, these findings suggest that Fe-CDs, in conjunction with an acidic and H_2O_2-rich tumor microenvironment, contribute to ferroptosis in 4T1 cells.

Lipid peroxidation is a hallmark of ferroptosis. To evaluate lipid peroxidation levels, a lipid peroxidation (LPO) assay was conducted, where green fluorescence intensity served as an indicator of peroxidation levels. As illustrated in Fig.4(D), negligible green fluorescence was observed in the control and H_2O_2-treated groups, suggesting minimal LPO. In contrast, Fe-CD-treated 4T1 cells exhibited significantly increased green

fluorescence, confirming the occurrence of lipid peroxidation. Notably, the Fe-CDs and H_2O_2 co-incubation group displayed the most intense green fluorescence, indicating the highest level of LPO. As a critical regulator of ferroptosis, GPX4 depletion leads to unchecked lipid peroxidation and subsequent cell death. Western blot analysis[Fig.4(E)—(F)] revealed no significant difference in GPX4 expression between the control and H_2O_2-treated groups, indicating normal GPX4 activity. However, a substantial reduction in GPX4 expression was observed in the Fe-CD-treated group, and GPX4 protein bands were nearly undetectable in the Fe-CDs and H_2O_2 co-incubation group. This pronounced decrease in GPX4 expression further confirms the involvement of ferroptosis in Fe-CD-induced cell death.

In summary, Fe-CDs exhibit mitochondrial targeting properties and facilitate ROS generation within the tumor microenvironment. The resulting oxidative stress leads to mitochondrial membrane depolarization, exacerbates lipid peroxidation, and induces GPX4 downregulation, ultimately triggering ferroptosis. These findings provide valuable insights into the potential application of Fe-CDs in tumor therapy.

3.5 *In Vivo* Tumor Therapeutic Efficacy of Fe-CDs

Building on the promising *in vitro* therapeutic and mechanistic findings, we further evaluated the *in vivo* tumor treatment efficacy of Fe-CDs. A 4T1 tumor-bearing mouse model was established by subcutaneous injection of cancer cells[Fig.5(A)]. When tumors reached approximately 50 mm^3, mice were randomly divided into two groups: the control group and the Fe-CDs treatment group, with Fe-CDs administered *via* intratumoral

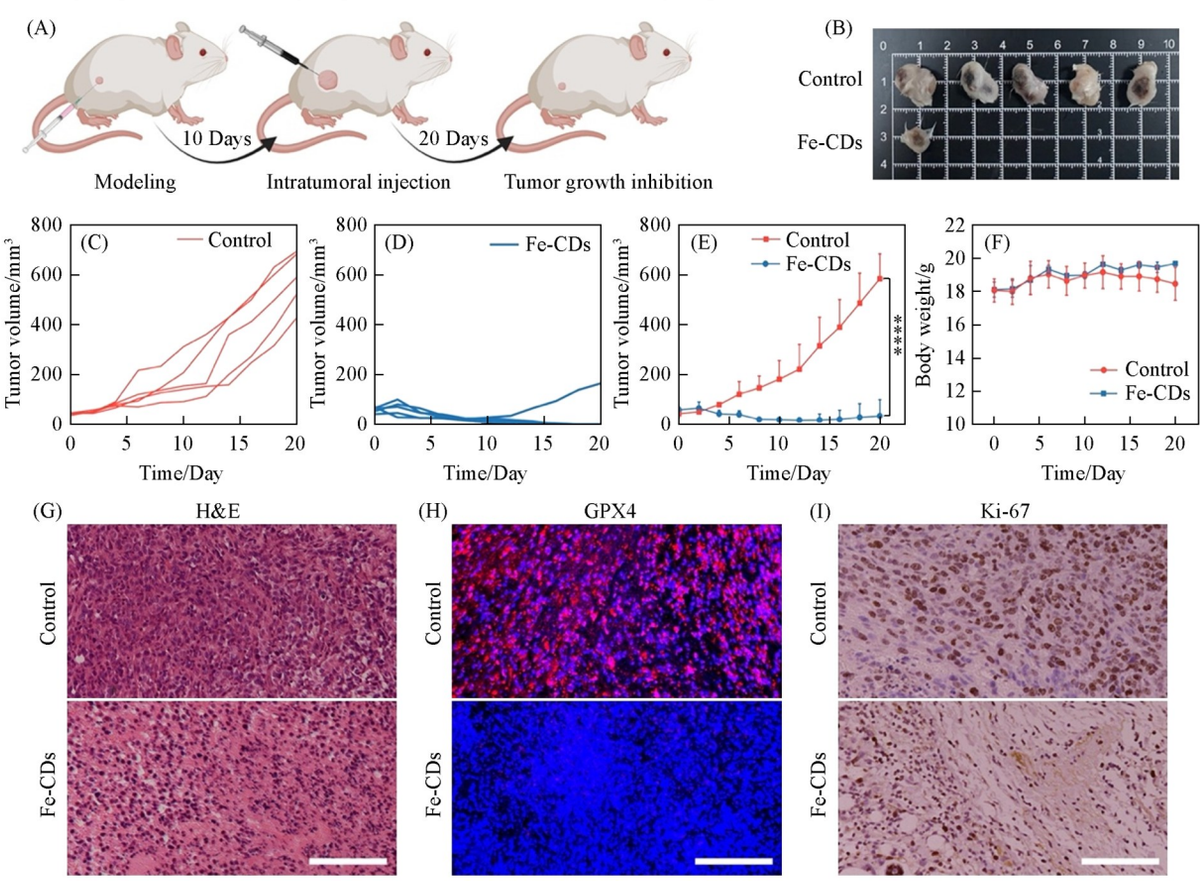

Fig. 5 *In vivo* tumor therapeutic efficacy of Fe-CDs

(A) Schematic illustration of the establishment of 4T1 tumor-bearing mice and the evaluation of Fe-CD therapy; (B—D) representative digital images of tumors and tumor growth curves for different treatment groups over 20 d; (E) average tumor volume of 4T1 tumor-bearing mice under various treatments; (F) changes in body mass over 20 d for different treatment groups; (G) H&E-stained tumor sections; (H) GPX4 immunofluorescence staining; (I) Ki67 immunohistochemical staining of tumors following different treatments; statistical analysis was performed using an unpaired *t*-test(*P<0.05, **P<0.01, ***P<0.001 and ****P<0.0001).

injection.

Tumor volume and body mass were recorded every two days over a 20-day period, after which all mice were sacrificed. Tumor excision revealed that mice in the control group exhibited significant tumor growth, whereas those treated with Fe-CDs showed substantial tumor suppression, with complete tumor eradication observed in 80% of the treated mice[Fig.5(B)]. The recorded tumor growth curves further confirmed this trend[Fig.5(C)—(E)]. This remarkable therapeutic outcome is attributed to the potent POD-mimicking activity of Fe-CDs, which generates hydroxyl radicals and induces ferroptosis in 4T1 cells.

The histological analysis provided additional evidence of Fe-CDs-induced ferroptosis. H&E staining of tumor sections from the control group displayed intact tumor morphology, whereas the Fe-CDs-treated group exhibited extensive cancer cell damage[Fig.5(G)]. Immunofluorescence staining for GPX4, labeled with green fluorescence, showed strong fluorescence in the control group, while only minimal fluorescence was detected in the Fe-CDs-treated group, indicating substantial ferroptosis induction[Fig.5(H)]. This suppression of tumor cell proliferation was further confirmed by Ki67 immunohistochemical staining[Fig.5(I)].

Additionally, no significant body mass loss was observed throughout the treatment[Fig.5(F)], and histopathological analysis of major organs(heart, liver, spleen, lungs, and kidneys) revealed no apparent damage (Fig.S5 in the ESI), demonstrating the excellent biocompatibility of Fe-CDs. Furthermore, hematological and biochemical analyses showed no significant differences in any parameters between the Fe-CDs-treated and control groups, further confirming the outstanding biocompatibility of Fe-CDs(Figs.S6 and S7 in the ESI).

4 Conclusions

In this study, we synthesized Fe-CDs with intrinsic red fluorescence and peroxidase-mimicking activity for tumor-specific catalytic therapy. Fe-CDs selectively accumulate in mitochondria, leveraging the acidic tumor microenvironment and excess hydrogen peroxide to generate hydroxyl radicals, inducing lipid peroxidation and ferroptosis. *In vitro* and *in vivo* experiments demonstrated strong tumor suppression, with complete eradication in 80% of treated mice. Histological and immunofluorescence analyses confirmed ferroptosis-mediated cell death, while biocompatibility assessments showed no significant systemic toxicity. By integrating fluorescence imaging with catalytic therapy, Fe-CDs offer a promising nanoplatform for precision tumor treatment and ferroptosis research.

The Supporting Information of this paper see http://www.cjcu.jlu.edu.cn/CN/10.7503/cjcu20250094.

参 考 文 献

[1] Gao L., Zhuang J., Nie L., Zhang J., Zhang Y., Gu N., Wang T., Feng J., Yang D., Perrett S., Yan X., *Nature Nanotechnology*, **2007**, *2*(9), 577—583
[2] Gao L., Wei H., Dong S., Yan X., *Advanced Materials*, **2024**, *36*(10), 2305249
[3] Gao S., Lin H., Zhang H., Yao H., Chen Y., Shi J., *Advanced Science*, **2019**, *6*(3), 1801733
[4] Yang B., Shi J., *Journal of the American Chemical Society*, **2020**, *142*(52), 21775—21785
[5] Wang M., Huang G., You Z., Jia R., Zhong Y., Bai F., *Chem. Res. Chinese Universities*, **2023**, *39*(4), 612—623
[6] Wang W., Luo Q., Li J., Li L., Li Y., Huo X., Du X., Li Z., Wang N., *Advanced Functional Materials*, **2022**, *32*(36), 2205461
[7] Liu B., Liu J., *Nano Research*, **2017**, *10*(4), 1125—1148
[8] Huang L., Chen J., Gan L., Wang J., Dong S., *Science Advances*, **2019**, *5*(5), eaav5490
[9] Cao M., Xing X., Shen X., Ouyang J., Na N., *Chem. Res. Chinese Universities*, **2024**, *40*(2), 202—212
[10] Huo M., Wang L., Wang Y., Chen Y., Shi J., *ACS Nano*, **2019**, *13*(2), 2643—2653
[11] Fan K., Xi J., Fan L., Wang P., Zhu C., Tang Y., Xu X., Liang M., Jiang B., Yan X., Gao L., *Nature Communications*, **2018**, *9*(1), 1440
[12] Otasevic V., Vucetic M., Grigorov I., Martinovic V., Stancic A., *Oxidative Medicine and Cellular Longevity*, **2021**, *2021*(1), 5537330
[13] Xie Y., Hou W., Song X., Yu Y., Huang J., Sun X., Kang R., Tang D., *Cell Death & Differentiation*, **2016**, *23*(3), 369—379

[14] Dixon S. J., Lemberg K. M., Lamprecht M. R., Skouta R., Zaitsev E. M., Gleason C. E., Patel D. N., Bauer A. J., Cantley A. M., Yang W. S., Morrison B., Stockwell B. R., *Cell*, **2012**, *149*(5), 1060—1072
[15] Wang H., Lin D., Yu Q., Li Z., Lenahan C., Dong Y., Wei Q., Shao A., *Frontiers in Cell and Developmental Biology*, **2021**, *9*, 629150
[16] Chen X., Comish P. B., Tang D., Kang R., *Frontiers in Cell and Developmental Biology*, **2021**, *9*, 637162
[17] Wu A., Han M., Ding H., Rao H., Lu Z., Sun M., Wang Y., Chen Y., Zhang Y., Wang X., Chen D., *Chemical Engineering Journal*, **2023**, *474*, 145920
[18] Ragazzon G., Cadranel A., Ushakova E. V., Wang Y., Guldi D. M., Rogach A. L., Kotov N. A., Prato M., *Chem*, **2021**, *7*(3), 606—628
[19] Shi Y., Xu H., Yuan T., Meng T., Wu H., Chang J., Wang H., Song X., Li Y., Li X., Zhang Y., Xie W., Fan L., *Aggregate*, **2022**, *3*(3), e108
[20] Wang B., Lu S., *Matter*, **2022**, *5*(1), 110—149
[21] Hussain M. M., Khan W. U., Ahmed F., Wei Y., Xiong H., *Chemical Engineering Journal*, **2023**, *465*, 143010
[22] Li J., Yang S., Deng Y., Chai P., Yang Y., He X., Xie X., Kang Z., Ding G., Zhou H., Fan X., *Advanced Functional Materials*, **2018**, *28*(30), 1870206
[23] Xia C., Zhu S., Feng T., Yang M., Yang B., *Advanced Science*, **2019**, *6*(23), 1901316
[24] Nan F., Xue X., Li J., Liang K., Wang J., Yu W. W., Ge J., Wang P., *Science China Materials*, **2024**, *67*(11), 3742—3752
[25] Wang X., Lu Y., Hua K., Yang D., Yang Y., *Analytical and Bioanalytical Chemistry*, **2021**, *413*(5), 1373—1382
[26] Yang M., Li H., Liu X., Huang L., Zhang B., Liu K., Xie W., Cui J., Li D., Lu L., Sun H., Yang B., *Journal of Nanobiotechnology*, **2023**, *21*(1), 431
[27] Deng Z., Qian Y., Yu Y., Liu G., Hu J., Zhang G., Liu S., *Journal of the American Chemical Society*, **2016**, *138*(33), 10452—10466
[28] Nan F., Jia Q., Xue X., Wang S., Liu W., Wang J., Ge J., Wang P., *Biomaterials*, **2022**, *284*, 121495
[29] Lu S., Sui L., Liu J., Zhu S., Chen A., Jin M., Yang B., *Advanced Materials*, **2017**, *29*(15), 1603443
[30] Li J., Wang J., Liang K., Xue X., Chen T., Gao Z., Ren H., Gao L., Ge J., *Chemical Engineering Journal*, **2024**, *500*, 157033
[31] Yang Y., Xu J., Zhou R., Qin Z., Liao C., Shi S., Chen Y., Guo Y., Zhang S., *Carbon*, **2024**, *219*, 118831
[32] Xie M., Li F., Li Y., Qian K., Liang Y., Lei B., Liu Y., Cui J., Xiao Y., *Chemical Engineering Journal*, **2025**, *506*, 159956
[33] Jiang B., Duan D., Gao L., Zhou M., Fan K., Tang Y., Xi J., Bi Y., Tong Z., Gao G. F., Xie N., Tang A., Nie G., Liang M., Yan X., *Nature Protocols*, **2018**, *13*(7), 1506—1520
[34] Huo M., Wang L., Chen Y., Shi J., *Nature Communications*, **2017**, *8*(1), 357

(Ed.: F, K)